Role of thermocline–SST coupling in the evolution of IOD events and their regional impacts

Aditi Deshpande · J. S. Chowdary ·
C. Gnanaseelan

Abstract The evolution of sea surface temperature (SST) and thermocline (represented by 20 °C isotherm depth, D20) in the east equatorial Indian Ocean (EIO) associated with the Indian Ocean Dipole (IOD) years is studied for the period of 50 years from 1958 to 2007. A new IOD index based on combined anomalies of surface winds, D20 and SST over the equatorial Indian Ocean is defined to identify strong and weak IOD events. It is found that the evolution of strong IOD events is driven by ocean dynamics in the form of thermocline–SST coupling and is strongly inter-active with the atmosphere, whereas the weak IOD events are mere response to surface winds without such dynamical coupling. The easterly wind anomalies extend up to the western equatorial Indian Ocean (WIO) during strong IOD years and support enhanced EIO air–sea interactions. On the other hand, the evolution of zonal wind anomalies is weak during the weak IOD years. Thermocline–SST coupling is robust in both EIO and WIO during strong IOD years, which is primarily responsible for the enhanced SST gradient, strong enough to establish anomalous Walker circulation within the Indian Ocean. The strong convection over the WIO associated with the Indian Ocean Walker cell triggers a secondary cell with subsidence over the African landmass. This double cell structure over the equatorial Indian Ocean is not reported before. Such double cell structure is not evident in weak IOD years and instead the convection over WIO extends up to African landmass. These are well supported by the spatial pattern of anomalous precipitable water during strong and weak IOD years. Strengthening of monsoon flow and local Hadley cell associated with strong IOD events enhances precipitation over the Indian subcontinent, whereas weak IOD years have less impact on the Indian summer monsoon circulation and rainfall. Analysis reveals that the EIO thermocline index and combined index could be potential predictors for the central Indian rainfall during summer.

1 Introduction

Indian Ocean (IO) Dipole (IOD) is the prominent coupled climate mode in the tropical IO and is phase locked to the seasonal cycle (Saji et al. 1999; Webster et al. 1999). IOD is characterised by strong east–west sea surface temperature (SST) anomaly gradient and upwelling favourable alongshore winds in the southeastern tropical IO from boreal spring which peak in September–November (SON; Saji et al. 1999). The magnitude of a given IOD event is estimated by Dipole Mode Index (DMI), which is the normalised time series of the difference in the SST anomalies between west equatorial IO (WIO; 50°E–70°E, 10°S–10°N) and east equatorial IO (EIO; 90°E–110°E, 10°S–Equator; Saji et al. 1999). Several studies have addressed the coupled atmospheric and oceanic response of IOD in terms of different indices such as SST anomalies over various regions (Webster et al. 1999), outgoing longwave radiation (OLR) anomalies, and wind anomalies (Gadgil et al. 2004). Annamalai et al. (2003) used indices based on 20 °C isotherm depth (D20) anomalies, equatorial wind index; alongshore wind anomalies off Java–Sumatra and SST anomalies over EIO to study the initiation or triggering mechanism of IOD. Several studies have attributed the triggering of IOD events to El Niño/Pacific forcing (e.g. Annamalai et al. 2003; Dommenget 2011). The trigger time, duration and evolution of anomalies also change from one event to another (Annamalai et al. 2003;

A. Deshpande · J. S. Chowdary · C. Gnanaseelan (✉)
Indian Institute of Tropical Meteorology, Pune 411 008, India
e-mail: seelan@tropmet.res.in

Meyers et al. 2007; Thompson et al. 2009; Du et al. 2012 and references therein).

The EIO region is a part of the Indo-Pacific warm pool and is characterised by strong convection throughout the year (Saji et al. 1999; Webster et al. 1999). During an IOD year however, this convection shifts to the west due to strong cooling over the eastern region and the presence of warm SST anomalies in the WIO. This gives rise to an anomalous Walker circulation with subsidence over EIO and convection over WIO leading to suppressed rainfall over Indonesia and excess rainfall over East Africa (Behera et al. 1999; Saji and Yamagata 2003; Yamagata et al. 2004). El Niño in its developing phase induces negative rainfall anomalies over the Indian subcontinent during June–September (JJAS), whereas enhanced rainfall is experienced during most of the IOD years. IOD weakens the El Niño impact over tropical IO and most of the El Niño–IOD co-occurrence events are associated with normal Indian summer monsoon (ISM) rainfall (Ashok et al. 2004).

The coupled processes associated with IOD begin with the eastern cooling (Saji et al. 1999). The cooling in the EIO is accompanied by thermocline shoaling and the intensity/amplitude of the IOD event can be represented by the magnitude of thermocline variations (Murtugudde et al. 2000). The upwelling in the EIO is generally triggered by wind forcing, though variations in mixed layer depth and barrier layer depth modulate the dynamic response (Vinayachandran et al. 1999; Thompson et al. 2006).

Most of the above studies have focussed on the initiation, impact of IOD on regional climate and IOD–El Niño relationship. The current study however emphasizes the differences in the evolution patterns of IODs which occurred between 1958 and 2007 using reanalysis products. Nine IOD events [pure IOD and IOD–El Niño co-occurrence years (Table 1)] were reported during the study period. The impact of IOD events which are coupled to the thermocline and those that are not coupled are distinct. These are evident in the circulation features and the associated modulation in different fields. The present study is focussed on understanding these differences, identifying strong and weak IOD years and their impact on regional climate. We also considered the evolution of various oceanic and atmospheric parameters to explore the IOD initiation, mechanism, their characteristics and regional impacts. Rest of the paper is organised as follows. Section 2 presents data and methodology used in the study; thermocline–SST coupling and their response to strong and weak IOD forcing are addressed in Sect. 3. The atmospheric response to the anomalous events is discussed in Sect. 4. Finally, Sect. 5 summarises the major findings.

2 Data and methodology

Monthly means of Simple Ocean Data Assimilation (SODA) (Carton and Giese 2008) temperature and European Centre for Medium Range Forecasting (ECMWF) Reanalysis, (ERA) ERA-40 (Uppala et al. 2005) and ERA-Interim (Dee et al. 2011) winds (surface to 100 mb level) over a period of 50 years (1958–2007) are used for the analysis. The depth of 20 °C isotherm (representative of thermocline depth) is computed using SODA temperature field, and is denoted as D20 throughout the study. In addition, precipitable water from ERA-40/ERA-Interim and gridded rainfall data from Aphrodite (Yatagai et al. 2012) over the period of 1958–2007 are also used. Incoming shortwave radiation and latent heat flux from ERA-40 reanalysis (1958–2002) and Tropflux (2002–2007) (Praveen Kumar et al. 2012) are also used to investigate the evolution of fluxes associated with the convection (subsidence) over western (eastern) tropical IO during strong and weak years.

The alongshore winds along the coast of Sumatra are computed using ERA surface winds by considering an angle of 135° with the horizontal plane (Susanto et al. 2001). The anomalies of different fields are computed by subtracting the respective monthly climatology and are detrended by removing the linear trend over the study period. Statistical methods such as correlation and composite analysis are used to understand the physical mechanisms.

DMI, normalised D20 anomalies averaged over EIO region (D20 index), and normalised zonal wind anomalies similar to the index used by Gadgil et al. (2004) averaged over the equatorial region, 60°E–90°E, 2°S–2°N (wind index) and a combined index based on the above three indices are used to classify strong and weak IOD events. The combined index is formulated as follows:

$$Combined\ Index = \frac{DMI - D20\ Index - Wind\ Index}{3.0}$$

An IOD year is classified as a strong year when each of the three indices DMI, D20 index and wind index exceeds one standard deviation during SON, and the combined index exceeds two-standard deviation. When either of the above three indices are within the range of half to one standard deviation, and the combined index is between one and two standard deviation during SON, the year is classified as a weak IOD year. List of strong and weak IOD years is given in Table 1.

Table 1 List of strong and weak IOD years

Strong IOD years	Weak IOD years
1961, 1994, 1997[a], 2006[a]	1963[a], 1967, 1972[a], 1977, 1982[a]

[a] El Niño–IOD co-occurrence years

3 Role of oceanic and atmospheric processes in IOD evolution

Figure 1a illustrates the time series of different indices of IOD (DMI, D20 and wind indices) over the period of 1958–2007. These indices reveal that DMI has robust positive peaks during IOD events, whereas D20 and wind indices display negative peaks. The current definitions of IOD do not adequately explain the processes associated with the developing phase of IOD, but it is well established that the developing phase of IOD influences ISM rainfall (Ashok et al. 2001). DMI focuses on the zonal gradients of SST anomalies. However, this index is significant even without western warming/cooling (e.g. 1997/1998), which is one of its drawbacks. Further studies have pointed out that SST anomalies of the western and eastern IO are not significantly anticorrelated (e.g. 1963, 1994) (Allan et al. 2001; Annamalai et al. 2003). In addition to that, the western warming is not confined to the same region during each IOD event, whereas the cooling over eastern pole occurs over the same region during each event (Saji and Yamagata 2003). Hence it is important to emphasize the oceanic processes which are responsible for the evolution of SST anomalies over equatorial IO. So an index is derived based on the thermocline, wind and SST anomalies to depict the regional climate variability associated with IOD in this study. The importance of this combined index is demonstrated in Sect. 4. We begin by evaluating the relationship between different indices. A strong correlation of −0.74 (−0.88) is noted between DMI and D20 index (wind index) during SON period. The D20 index and wind index are also strongly correlated (0.88) with each other during SON. All correlations are significant at 95 % confidence level based on the two tailed t test. This indicates the existence of strong relationship among D20, wind and SST anomalies which further justifies the formulation of the new combined index.

Figure 1b, c show the evolution of SST and D20 anomalies respectively over the EIO region. The shoaling of D20 anomalies in this region is stronger and evolves early during strong IOD years as compared to weak IOD years. During strong years, D20 shoals by 10–50 m, while during weak years; D20 shoaling is <10 m and is limited to the peak phase of IOD. The SST anomalies over the EIO region during strong IOD years show enhanced cooling in the range of about 1–2 °C, which begins in early summer (June–July) and reaches its maximum during SON. In contrast, the cooling during the weak years is <1 °C, and significant anomalies are seen only for a shorter time period (SON). In particular, the differences in the evolution and magnitude of the anomalies are evident in the composites of SST and D20 (Fig. 1d, e).

In addition to SST response, alongshore wind anomalies (along the coast of Java–Sumatra), equatorial wind anomalies and thermocline response are known to be important components of IOD (Saji et al. 1999; Annamalai et al. 2003). Figure 1d, e show the composite evolution of anomalous alongshore winds (along the coast of Sumatra), equatorial wind anomalies and the associated D20 and SST anomalies during strong and weak IOD years respectively. In the case of strong years, coherent evolution of alongshore winds, D20 and SST (over EIO) is evident from May onwards. The SST responds to the thermocline shoaling and the resultant cooling starts in July. It is important to note that the coherent shoaling of thermocline (D20 anomalies) corresponding to the consistent strengthening of alongshore winds with time is a prominent feature of strong IOD years. This reveals a strong coupling between alongshore winds and thermocline through coastal upwelling/ entrainment feedback. This positive feedback maintains negative SST anomalies over EIO (e.g. Li et al. 2003; Spencer et al. 2005), suggesting the existence of strong thermocline–SST coupling. In contrast, during weak years, the alongshore wind anomalies are weaker and their magnitude remains more or less constant from June to December (Fig. 1e). Therefore, such wind–thermocline– SST feedback is not established in weak years especially during the developing phase of IOD. This is also evident in the evolution of equatorial wind anomalies (Fig. 1d, e). Our analysis reveals that the thermocline shoaling in response to alongshore winds begins from early summer during the strong IOD years as compared to weak years.

Evolution of the spatial patterns of D20 and SST anomalies also differs during strong and weak IOD years. This is demonstrated through the Hovmuller diagram of the SST and D20 anomalies averaged over 10°S–Equator (Fig. 2). A distinct feature of all the strong IOD years is the westward phase propagation of deepening thermocline and warm SST anomalies through central to western IO. These features are rather inconsistent during the weak years, with western warming apparent only towards the end of the calendar year. Deepening of the thermocline in the WIO is more intense in strong IOD years compared to the weak IOD years suggesting that the oceanic processes are responsible for the western warming. In contrast, the eastern cooling during weak events is significantly less compared to that of strong events, and so an intense east– west SST gradient is not set up even during the peak phase of IOD. The zonal gradient in D20 anomalies also reveals similar picture, whereas both SST and D20 anomalies display well organised intense east–west gradient during strong IOD years since the developing phase. The consistent evolution of D20 anomalies over EIO during strong IOD years suggests its possible use as a predictor. During strong IOD years, evolution of SST is consistent with that of thermocline, suggesting a stronger coupling between them in both WIO and EIO.

Fig. 1 **a** IOD indices-Dipole Mode Index (*black*) overlaid with D20 index (*red*) and wind index (*blue*), **b** SST anomalies (°C, averaged over EIO), **c** D20 anomalies (m, averaged over EIO), **d** Composites of D20 anomalies (*black*, m), SST anomalies (*red*, °C) averaged over EIO, alongshore wind anomaly along Sumatra coast (*blue*, ms^{-1}) and equatorial zonal wind anomalies averaged over 60°E–90°E, 2°S–2°N (*green*, ms^{-1}) during strong years, **e** is same as, **d** except for weak years
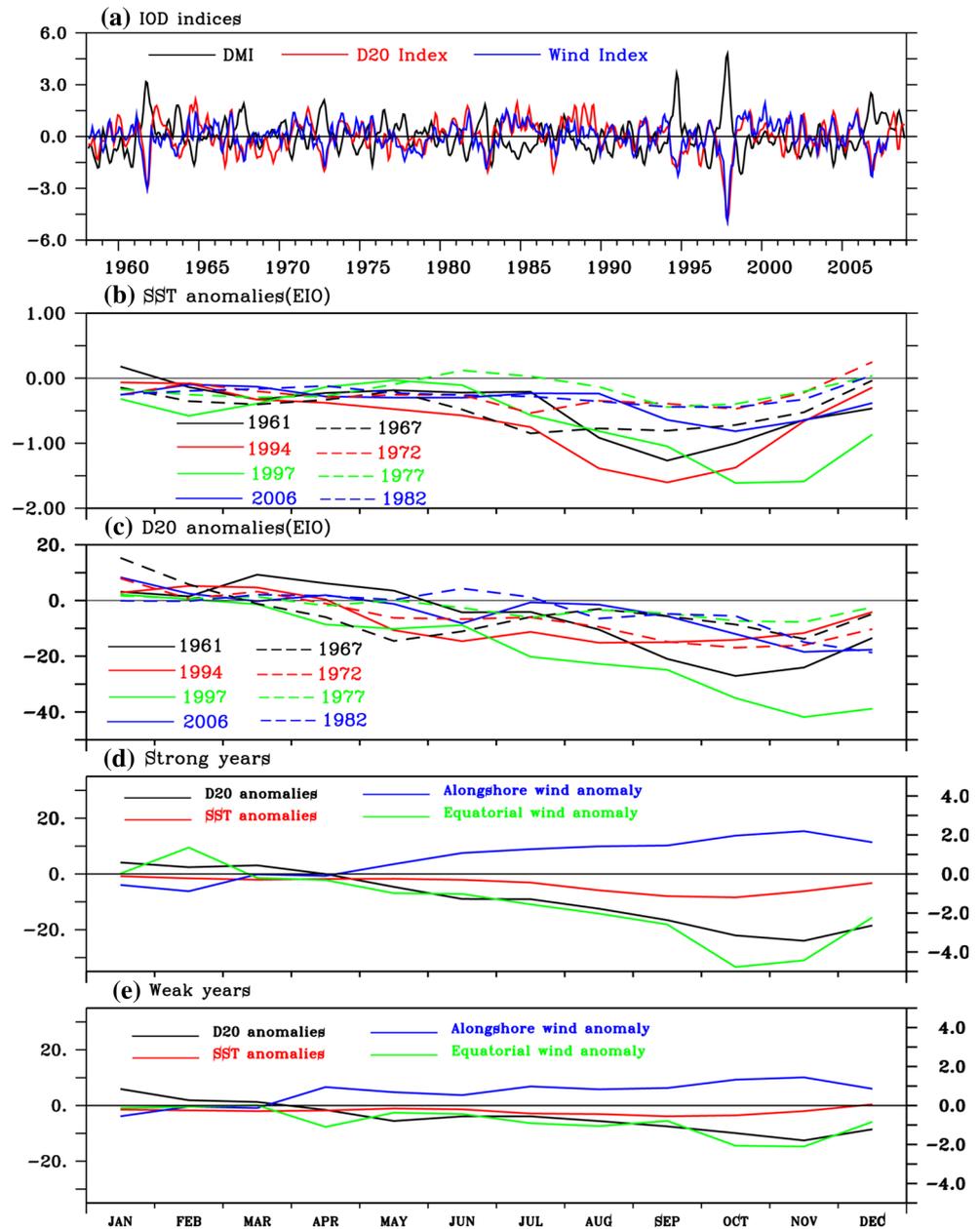
The evolution of vertical structure of temperature anomalies in strong and weak IOD years (Fig. 3) further explains the oceanic processes associated with the thermocline–SST coupling. Significant subsurface anomalies (cooling) are evident in strong years since May which strongly manifests at the surface (SST) by July (Fig. 3) and progresses consistently up to November (figure not shown). These negative SST anomalies further strengthen the alongshore winds through air–sea interaction in addition to the dynamical feedback. As discussed above, the intensity of eastern cooling (especially subsurface) is much robust in strong years since May. It is important to note that the subsurface temperature anomalies and their evolution (May onwards) are significant with larger spatial extent in the case of strong IOD years (Fig. 3). The evolution of this cooling is systematic and strongly supports the dynamical link from May to November. In case of weak IOD years such anomalous pattern or its evolution is absent. Similar differences in both the evolution and intensity of western warming are also evident (Fig. 3) during strong and weak years. The shoaling of mean isotherms to the east of 85°E is also apparent since June in strong years. However, systematic shoaling of isotherm/thermocline and surface cooling are not apparent in weak years.

The coherent evolution of thermocline and SST anomalies during strong IOD years (from developing phase to peak phase) is more evident in the composite (Fig. 4a). This coherent evolution is lacking during weak IOD years.

Fig. 2 Time–longitude plot of SST anomalies (*shaded*, °C) overlaid with D20 anomalies (*contours*, m) averaged over 10°S–Eq, during strong IOD years (*left panels*) and weak IOD years (*right panels*)
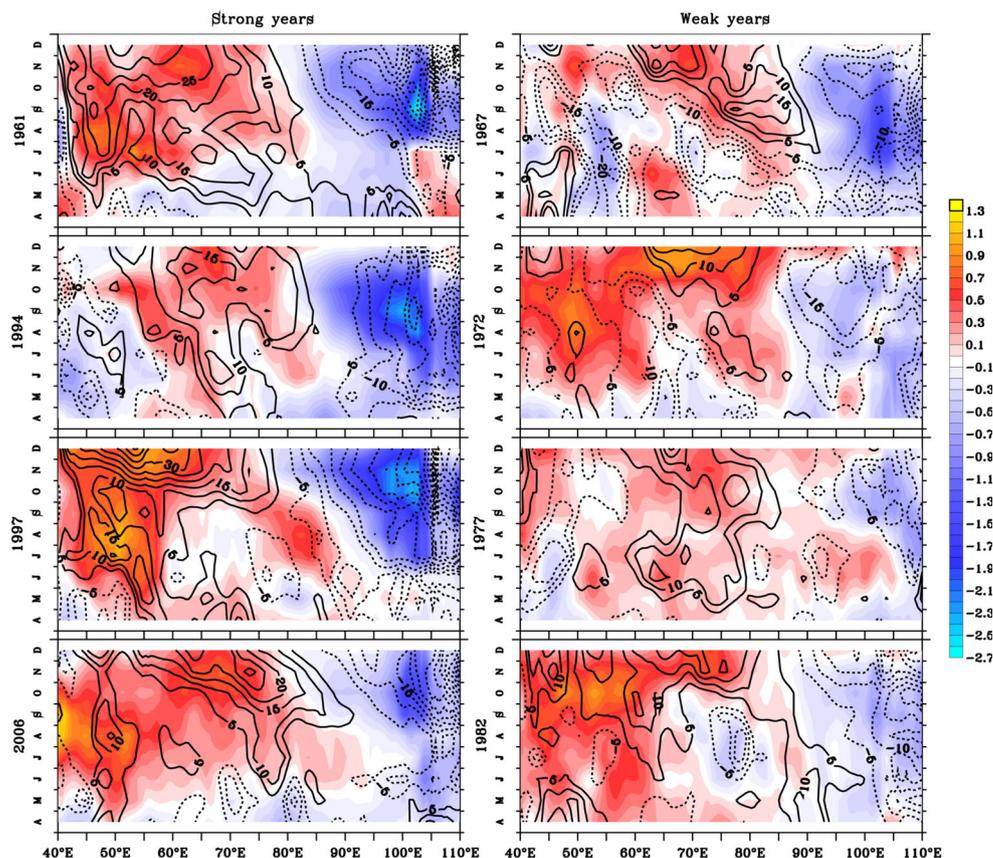
In this context it is important to examine the contribution of fluxes in the evolution of SST anomalies especially during the weak IOD years. SST cooling in the EIO during weak years is maintained by the wind–evaporation–SST (WES) feedback mechanism (Fig. 4d). The southeasterly wind anomalies off Sumatra enhance evaporation and the associated latent heat cooling. This feedback is primarily responsible for SST cooling as the thermocline–SST coupling is weak during weak years. On the other hand during strong IOD years, the EIO cooling is well explained by the ocean dynamical processes though WES feedback is active away from the Sumatra coast (Fig. 4c). The western warming during weak IOD years is mostly explained by the negative latent heat flux anomalies by reducing the evaporative cooling (Fig. 4d), whereas during strong years, it is explained by ocean dynamics. The subsidence induced by eastern cooling and the associated clear sky radiation are responsible for the positive shortwave radiation anomalies in the eastern IO while deep convective clouds manifest as negative anomalies in the west (Fig. 4c). These are in agreement with Chowdary and Gnanaseelan (2007). Such well organised pattern is not established during the weak IOD years.

The east–west gradient in SST anomalies in the equatorial IO is evident since summer during strong IOD years (Fig. 4a) whereas it is not evident in the weak years

(Fig. 4b). The anomalies peak in SON and are very robust during strong years. This zonal SST gradient supports easterly wind anomalies over the central equatorial region (Fig. 4e). In contrast, during weak IOD years, the winds are weaker in intensity. The strong anomalous winds and gradients in SST and thermocline suggest the establishment of Bjerknes (1969) feedback during the peak phase of strong years over the equatorial IO. In contrast, these processes are feeble in weak years mainly due to weak thermocline–SST relationship (Fig. 4b). The spatial extent and strength of surface wind anomalies affect atmospheric circulations during summer (June–August, JJA) and peak phase (SON) of IOD which is discussed in detail in the following section. Hereafter summer refers to the developing phase of IOD.

4 Anomalous circulation and precipitation patterns associated with IOD

Anomalous subsidence (convection) over EIO (WIO) is a prominent feature during the peak phase of IOD (Tokinaga and Tanimoto 2004; Chowdary and Gnanaseelan 2007). Strong subsidence over large region is an indicative of changes in the IO Walker circulation. The anomalous Walker circulation in SON is characterised by a double cell

Fig. 3 Depth longitude sections of subsurface temperature anomaly composites (*shaded*, °C) superimposed with temperature isotherms (*contours*, °C) averaged over 10°S–Eq from May to August (**a–d**) for strong IOD years and (**e–h**) for weak IOD years. The anomalies are standardized by dividing the composite by its monthly standard deviation and the standardized anomalies greater (less) than 0.5 (−0.5) are *shaded*
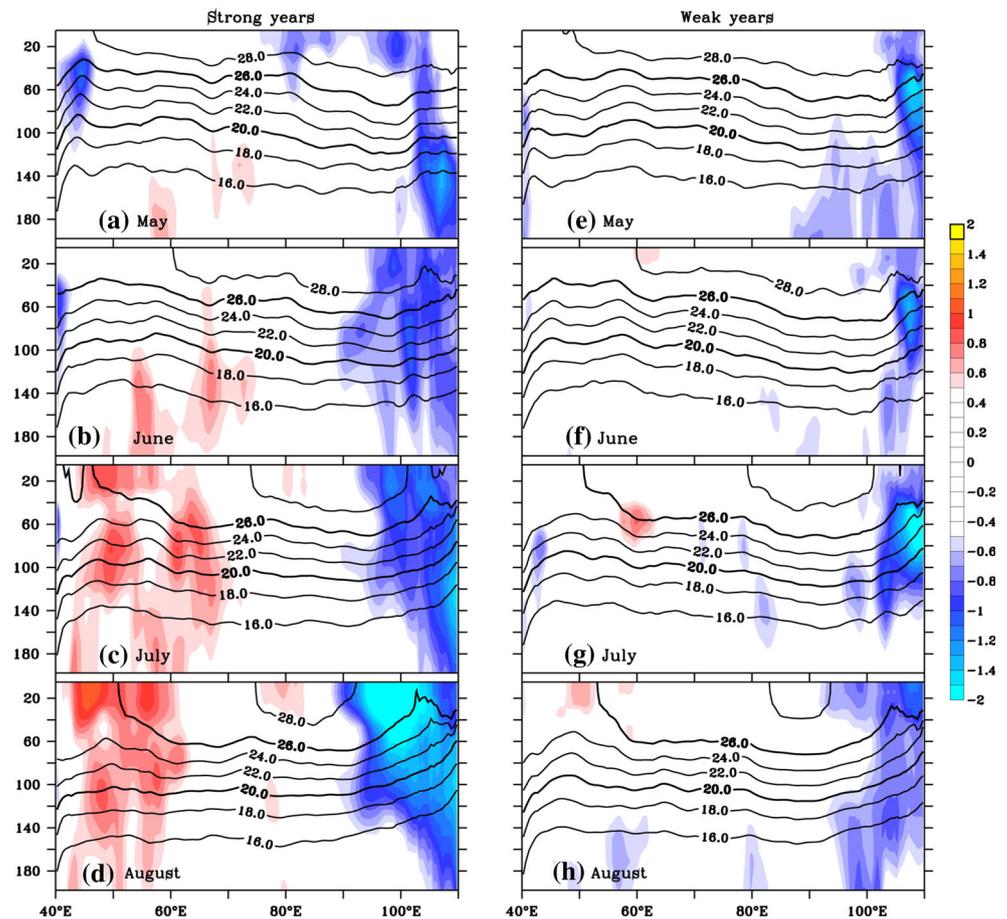
pattern (convection over WIO and subsidence over EIO and African landmass) during the strong IOD years (Fig. 5a). This pattern is well supported by the precipitation (precipitable water) anomalies (Fig. 5c). Such double cell pattern in the Walker circulation is absent during the weak IOD years, instead the convection is spread over WIO and Africa and subsidence is confined over EIO (Fig. 5b), which is reflected in the anomalous precipitable water as well (Fig. 5d). To the best of our knowledge, the double celled Walker circulation over the Indian oceanic rim has not been reported before. It is important to note that the upper level divergence around 60°E during the weak years is not associated with low level convergence and could be forced remotely. The interactions between El Niño, IOD and North Atlantic Oscillation could be contributing factors for such circulation patterns (e.g. Guan and Yamagata 2003 and references therein) which is beyond the scope of the present paper. Figure 5e, f show the spatial pattern of SST anomalies over Indo-Pacific region during SON. Though significant differences are not seen in the east Pacific SST anomalies, notable changes are evident over the IO. This change in SST pattern over the equatorial IO and the associated strong east–west gradient contribute to the differences in the Walker circulation

between strong and weak IOD years. The spatial pattern of east/central Pacific SST anomalies is similar during both weak and strong IOD years. This suggests that different flavors of El Niño and Southern Oscillation may have similar influence on both weak and strong IOD events. Moreover, both strong and weak IOD events co-occurred with strong El Niño (Table 1). This suggests that although El Niño like conditions may trigger IOD, the evolution of IOD is mainly governed by local ocean–atmosphere interactions (Yamagata et al. 2004).

While examining the evolution of the double Walker cell in the equatorial IO during the peak phase of IOD, it is found that these circulation features are evident from the preceding summer (Fig. 6). This has significant impact on the ISM as evident from Fig. 6c. During the weak IOD years, the spatial pattern of precipitable water shows an east–west orientation which is consistent with the circulation pattern. On the other hand, precipitable water anomalies during strong years are oriented meridionally, confining mostly over the narrow belt of convection (Fig. 6a, c). Another prominent difference between the strong and weak IOD years is the spatial distribution of ISM rainfall (Fig. 6c, d). The strengthened southwesterly surface wind anomalies of strong IOD years transport moist

Fig. 4 Time–longitude plot of SST anomaly composites (*shaded*, °C) overlaid with D20 anomalies (*contours*, m) averaged over 10°S–Eq, during **a** strong IOD years and **b** weak IOD years. Time–longitude plot of incoming shortwave flux anomaly composites (*shaded*, Wm^{-2}) overlaid with latent heat flux anomaly composites (*contours*, Wm^{-2}) averaged over 10°S–Eq, during **c** strong years and **d** weak years. Spatial distribution of sea surface height anomalies (*shaded*, cm) overlaid with surface wind anomalies (*vectors*, ms^{-1}) and SST anomalies (*contours*, °C) during September–November (SON) for **e** strong years and **f** weak years
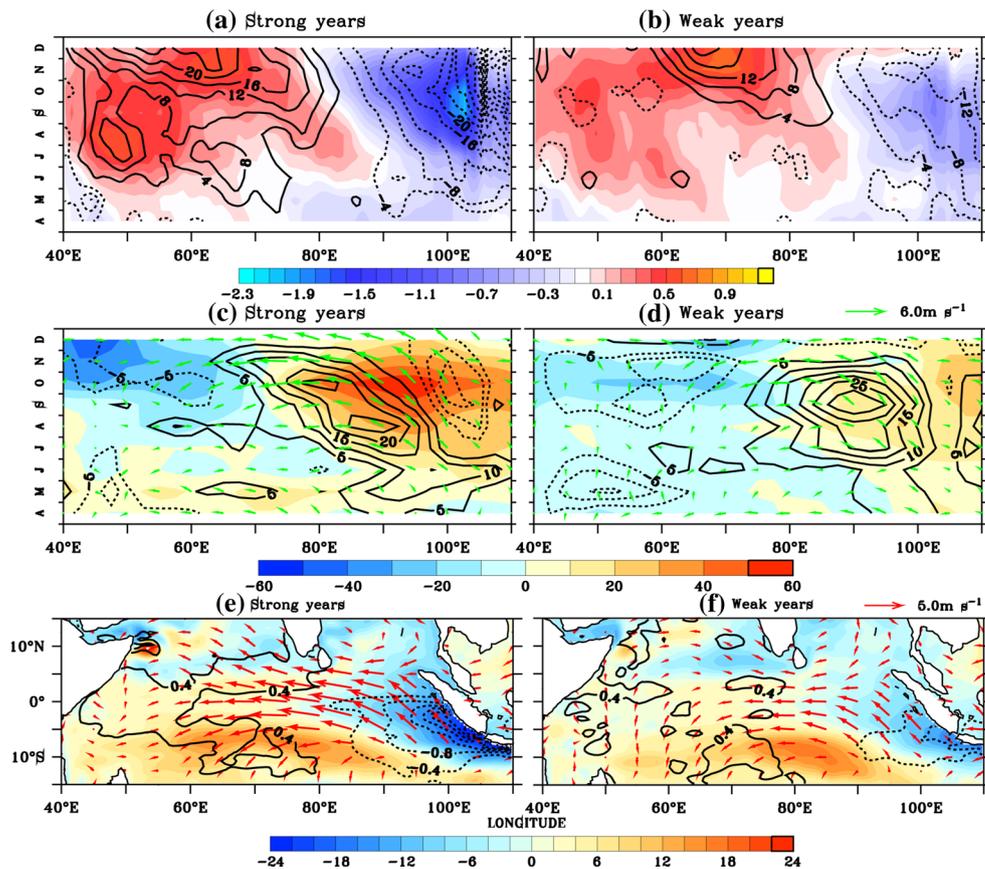
Fig. 5 Depth–longitude plot of wind divergence anomalies (*shaded*, ×10^{-7}, s^{-1}) overlaid with anomalous zonal (ms^{-1})–vertical (in −10^{-2} Pa s^{-1}) circulation averaged over 5°S–5°N during **a** strong IOD years, **b** weak IOD years. (*Middle panels*) Precipitable water (*shaded*, kg m^{-2}) overlaid with precipitation anomalies (*contours*, mm day^{-1}) during **c** strong years and **d** weak years. (*Lower panels*) Equatorial Indo-Pacific SST anomalies (*shaded*, °C) overlaid with D20 anomalies (*contours*, m) during **e** strong years and **f** weak years during September–November (SON)
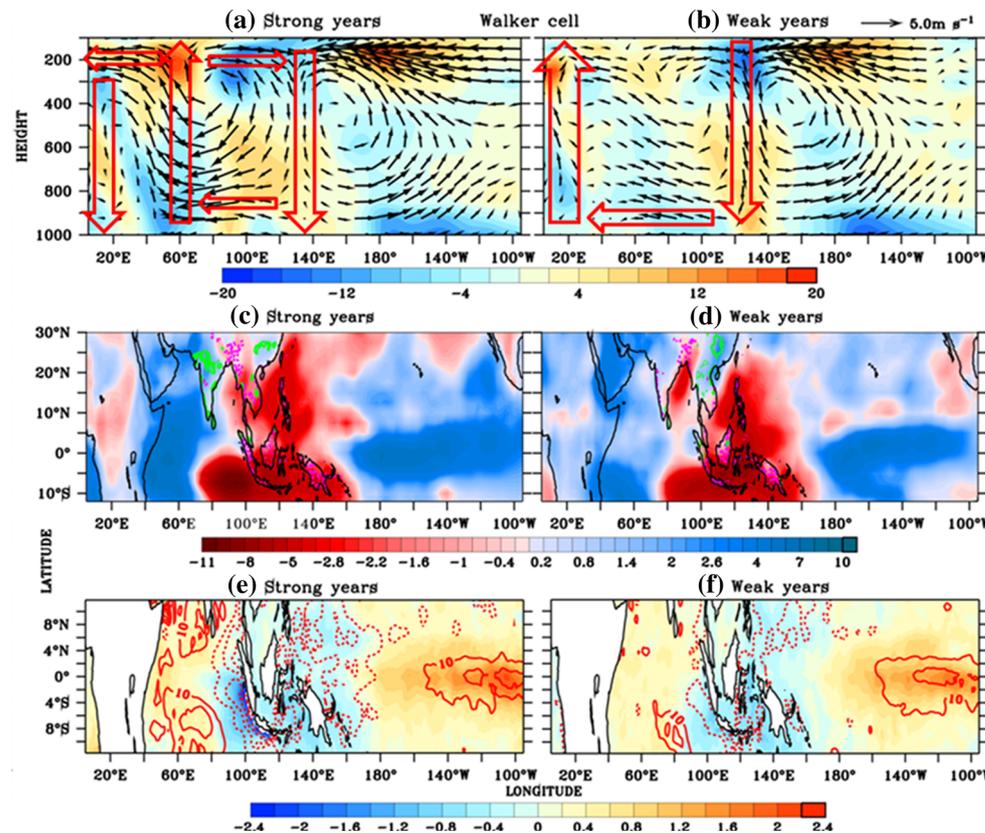
Fig. 6 Depth–longitude plot of wind divergence anomalies (*shaded*, $\times 10^{-7}$ s^{-1}) overlaid with anomalous zonal (in ms^{-1})–vertical (in -10^{-2} Pa s^{-1}) circulation averaged over during 5°S–5°N **a** strong IOD years, **b** weak IOD years. Composites of precipitable water (*shaded*, kg m^{-2}) overlaid with precipitation anomalies (*contours*, mm day^{-1}) and 850 mb wind anomalies (*vectors*, ms^{-1}) during **c** strong years and **d** weak years during June–August (JJA)
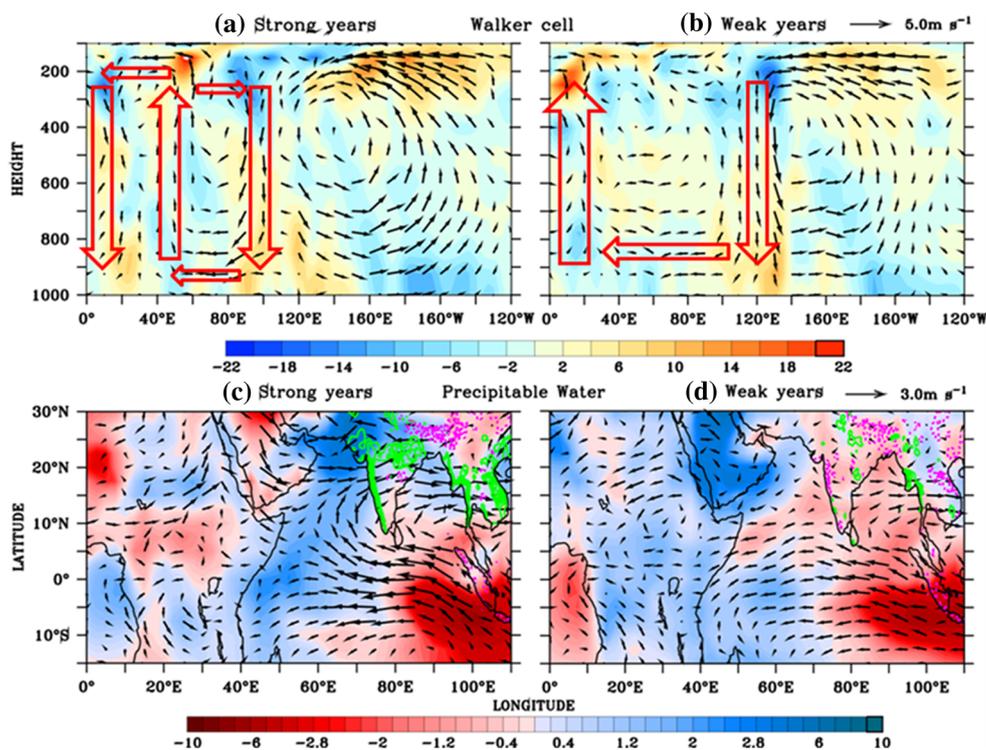
air towards the Western Ghats, enhancing rainfall over this region. The strengthening of winds over Arabian Sea and enhanced rainfall over the Western Ghats are the characteristic features of IOD (Annamalai et al. 2005; Izumo et al. 2008). However, we emphasize here that these organized patterns are evident only during the strong IOD years. The circulation pattern is not favourable for enhanced Western Ghats precipitation during weak IOD years owing to weak meridional winds.

During strong IOD years intensified rainfall is seen over central India and the Western Ghats (Fig. 6c). Figure 7a shows enhanced convection over the central India region and head Bay of Bengal (15°N–23°N) and subsidence over EIO during summer. This organised convection over Indian region is absent during weak years (Fig. 7b). Intense cooling in the EIO associated with thermocline–SST coupling primarily drives the anomalous Hadley circulation during strong years. The enhanced rainfall over central India is explained through the local Hadley circulation. This further strengthens the importance of EIO thermocline–SST coupling in modulating the atmospheric circulation. Overall, the impact of developing phase of IOD on ISM is significant only during the strong IOD years when the thermocline response is strong. To further strengthen our findings, we carried out correlation between the anomalous circulation (vertical–meridional section) with different IOD indices (Fig. 7c–f) during summer. It is evident that the

simultaneous correlation with D20 index shows a pattern closer to the strong IOD composite. This further supports our results.

We also carried out lead–lag correlation between anomalous July–August (JA) circulation with different indices of June as displayed in Fig. 8. The correlation with June D20 index (Fig. 8d) shows circulation pattern similar to the anomalous Hadley circulation of strong IOD years (Fig. 7a) suggesting EIO D20 as a useful predictor for the central India rainfall. Similar relationship is seen when correlated with May indices (figure not shown).

The impact of IOD on ISM has been discussed in several studies (Behera et al. 1999; Ashok et al. 2004; Yamagata et al. 2004). These studies have shown that the positive phase of IOD strengthens the monsoon flow and intensifies monsoon rainfall. We have shown that the enhanced monsoon flow is seen only during strong IOD years. Therefore, it is important to identify the predictable components of IOD. For this we examined the lead–lag correlation between different IOD indices and precipitation anomalies during summer. Figure 9 shows the one point correlation between June indices (DMI, D20 index, wind index, combined index) with JA precipitation anomalies over Asian summer monsoon region. DMI shows weak positive correlation with precipitation anomalies over the monsoon trough region. Negative correlation is seen over southern peninsular India and Java–Sumatra. However, strong positive correlations are explained by D20 index

Fig. 7 Depth–latitude plot of wind divergence anomaly composite (*shaded*, $\times 10^{-7}$ s^{-1}) overlaid with anomalous meridional (ms^{-1})–vertical (in -10^{-2} Pa s^{-1}) circulation averaged over 80°E–100°E during **a** strong IOD years, **b** weak IOD years. Correlation of JJA wind divergence anomalies (*shaded*) overlaid with correlation of anomalous JJA meridional–vertical circulation (*vectors*) with JJA **c** DMI, **d** D20 index (correlation is taken with negative sign), **e** wind index (correlation is taken with negative sign) and **f** combined index
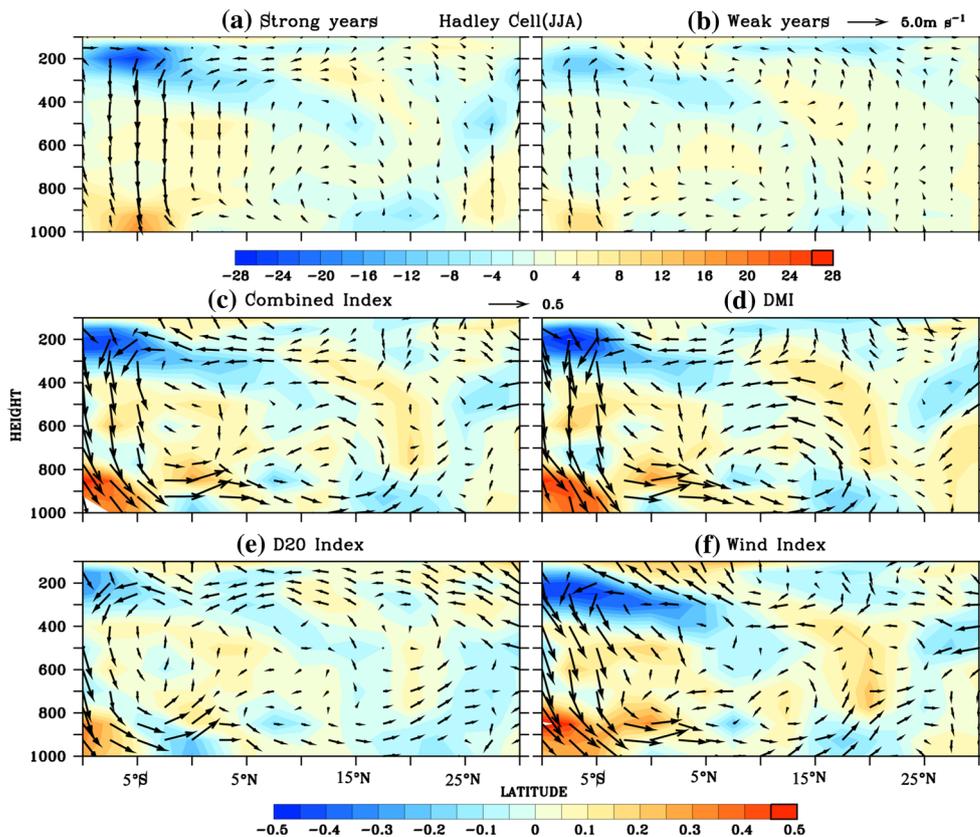
Fig. 8 **a** Combined IOD index during 1958–2007. Correlation of July–August wind divergence anomalies (*shaded*) overlaid with correlation of anomalous July–August meridional–vertical circulation (*vectors*) with June **b** DMI, **c** D20 index (correlation is taken with negative sign), **d** wind index (correlation is taken with negative sign) and **e** combined index averaged over 80°E–100°E
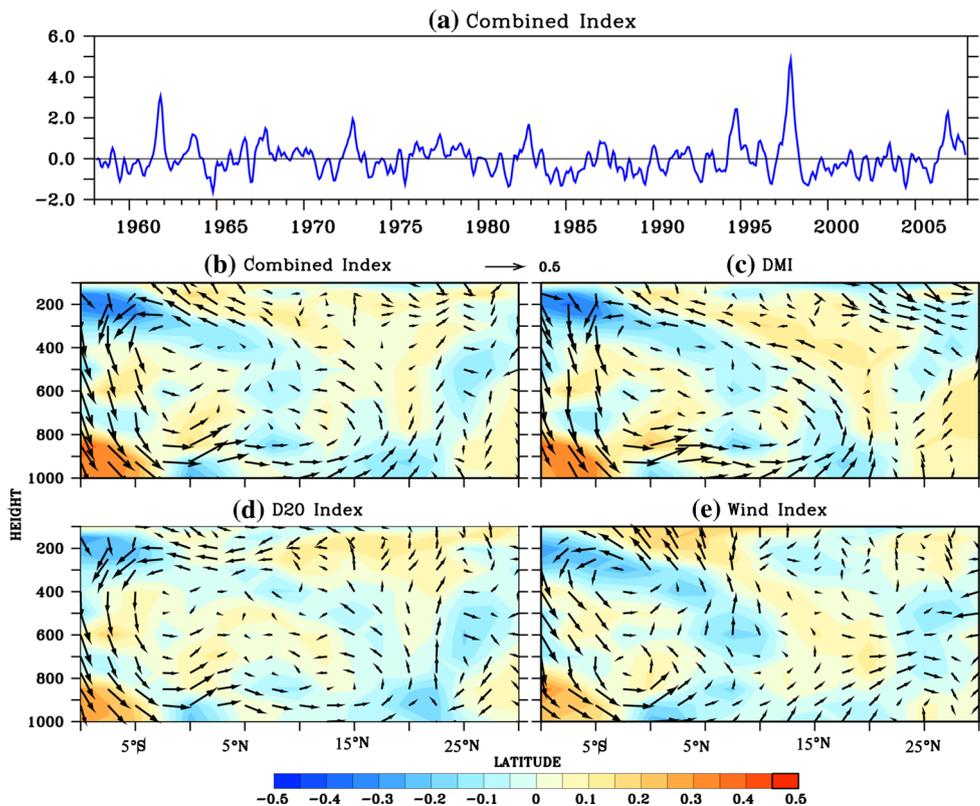
Fig. 9 Correlation of July–
August precipitation anomalies
from Aphrodite with June
a DMI, **b** D20 index (correlation
is taken with negative sign),
c wind index (correlation is
taken with negative sign) and
d combined index
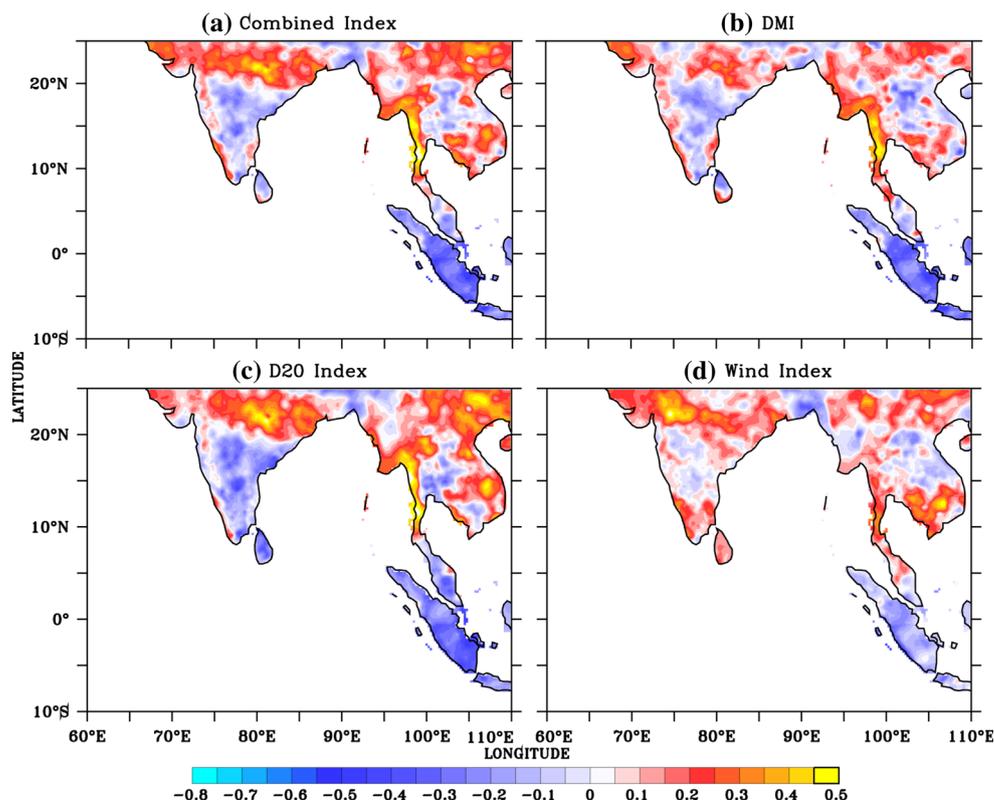
over the monsoon trough region as in the composites (Fig. 6c). The negative correlation over southern peninsular India and Java–Sumatra is also strong, indicating subsidence over these regions during IOD years. The wind index however showed much weaker signals. Since the combined index is representative of all the three indices, it revealed a pattern closer to the observed strong IOD composite (Fig. 6c). It is evident that D20 and combined index have the strongest lead correlation with precipitation anomalies (Fig. 9a, c), which shows the importance of thermocline–SST coupling and subsurface processes of equatorial IO in the climatic impact of IOD. This supports the hypothesis that thermocline based index as well as the combined index are important for regional climate prediction.

5 Summary and discussion

Indian Ocean Dipole induces significant anomalies in the seasonal circulation over the IO and the regional climate. However, the role of thermocline–SST coupling in the evolution of IOD and its regional impacts are not systematically examined in the past. We have formulated a new IOD index based on surface wind, D20 and SST anomalies. The strong and weak IOD years are classified using this index. The present study explores the dynamical coupling

in the equatorial IO region during the developing phase of strong and weak IOD years.

Coherent evolution of alongshore winds, D20 and SST in the EIO during strong IOD years supports strong coupling between alongshore winds and thermocline through coastal upwelling/entrainment feedback, which is evident since May. The SST anomalies evolve in response to the thermocline shoaling (since July), which is a prominent feature of strong IOD years. This is indicative of the thermocline–SST coupling during strong years. On the other hand, weak negative SST anomalies evolve in the EIO as a response to wind–evaporation–SST feedback during weak years. So we emphasize that the evolution of strong IOD events is driven by ocean dynamics and is coupled strongly to the atmosphere. However, such coupling is not apparent in the case of weak IOD years. Thermocline response and its co-evolution with SST is evident in both EIO and WIO during strong years. This establishes a strong east–west gradient in SST anomalies and the associated easterly wind anomalies over the central equatorial IO during strong years. The SST and wind response induces strong convection over WIO and subsidence over EIO. This triggers an anomalous double celled Walker circulation over IO with convection over WIO and subsidence over African landmass and EIO, which is not reported before. This anomalous double celled structure in the Walker circulation is absent during weak years.

The difference in strong and weak IOD years is also evident in the surface circulation. The westward extension of wind anomalies (easterlies) enhances the air–sea interaction over WIO region during strong IOD years which is weak during weak IOD years. The impact of differential IO forcing of strong and weak IOD years is reflected in the ISM rainfall patterns. Analysis reveals strengthened monsoon flow and enhanced precipitation over the Indian subcontinent (especially over the monsoon trough region) during strong IOD years (Fig. 7). The weak IOD years show less impact on summer monsoon rainfall. These differences in ISM response to strong and weak IOD events are not addressed in previous studies. The interaction between IOD and ISM occurs through changes in Hadley circulation driven by a thermocline response. The Hadley cell shows organized convection and convergence over land and strong subsidence over EIO in strong IOD years during the summer monsoon period. These circulation anomalies are weak during weak IOD years. The correlation analysis reveals that such anomalous Hadley circulation is closely related to thermocline evolution. To identify the predictable component of IOD, we carried out lead–lag correlation analysis of precipitation anomalies and different indices. The D20 index and combined index show strong correlation with Indian rainfall. Our analysis further demonstrates strong simultaneous correlation of these indices with Western Ghats rainfall (figure not shown).

This study concludes that a well defined dynamic coupling over the equatorial IO is seen only during strong IOD years, and hence thermocline variations should be accounted for, while determining the magnitude and impact of these events. The thermocline response in equatorial IO is a significant factor governing the evolution of IOD events and their impact on regional climate. Hence, our understanding of monsoon–IOD relationship can be improved by accounting for the equatorial IO thermocline response.

References

Allan NJ, Chambers D, Drosdowsky W, Hendon H, Latif M, Nicholls N, Smith I, Stone R, Tourre Y (2001) Is there an Indian Ocean Dipole, and is it independent of El Niño-Southern Oscillation? CLIVAR Exch 6:18–22

Annamalai H, Murtugudde R, Potemra J, Xie S-P, Liu P, Wang B (2003) Coupled dynamics over the Indian Ocean: spring initiation of the zonal mode. Deep Sea Res Part 2 50:2305–2330

Annamalai H, Liu P, Xie S-P (2005) Southwest Indian Ocean SST variability: its local effect and remote influence on Asian monsoons. J Clim 18:4150–4167

Ashok K, Guan Z, Yamagata T (2001) Impact of the Indian Ocean dipole on the relationship between the Indian monsoon rainfall and ENSO. Geophys Res Lett 28:4499–4502

Ashok K, Guan Z, Saji NH, Yamagata T (2004) Individual and combined influences of the ENSO and Indian Ocean Dipole on the Indian summer monsoon. J Clim 17:3141–3155

Behera SK, Krishnan R, Yamagata T (1999) Unusual ocean–atmosphere conditions in the tropical Indian Ocean during 1994. Geophys Res Lett 26:3001–3004

Bjerknes J (1969) Atmospheric teleconnections from the equatorial Pacific. Mon Weather Rev 97:163–172

Carton JA, Giese BS (2008) A reanalysis of ocean climate using Simple Ocean Data Assimilation (SODA). Month Weather Rev 136:2999–3017

Chowdary JS, Gnanaseelan C (2007) Basin wide warming of the Indian Ocean during El Niño and Indian Ocean dipole years. Int J Climatol 27:1421–1438. doi:10.1002/joc.1482

Dee DP et al (2011) The ERA-Interim reanalysis: configuration and performance of the data assimilation system. Q J R Meteorol Soc 137:553–597

Dommenget D (2011) An objective analysis of the observed spatial structure of the tropical Indian Ocean SST variability. Clim Dyn 36:2129–2145

Du Y, Cai W, Wu Y (2012) A new type of the Indian Ocean Dipole since the mid-1970s. J Clim 26:959–972

Gadgil S, Vinayachandran PN, Francis PA, Gadgil S (2004) Extremes of the Indian summer monsoon rainfall, ENSO and equatorial Indian Ocean oscillation. Geophys Res Lett 31:L12213. doi:10.1029/2004GL019733

Guan Z, Yamagata T (2003) The unusual summer of 1994 in East Asia: IOD teleconnections. Geophys Res Lett 30:1544. doi:10.1029/2002GL016831

Izumo T, de Boyer Montegut C, Luo JJ, Behera SK, Masson S, Yamagata T (2008) The role of the western Arabian Sea upwelling in Indian monsoon rainfall variability. J Clim 21:5603–5623

Li T, Wang B, Chang C-P, Zhang Y (2003) A theory for the Indian Ocean Dipole–zonal mode. J Atmos Sci 60:2119–2135

Meyers G, McIntosh P, Pigot L, Pook M (2007) The years of El Niño, La Niña, and interactions with the tropical Indian Ocean. J Clim 20:2872–2880. doi:10.1175/JCLI4152.1

Murtugudde R, McCreary JP, Busalacchi AJ (2000) Oceanic processes associated with anomalous events in the Indian Ocean with relevance to 1997–1998. J Geophys Res 105(C2):3295–3306. doi:10.1029/1999JC900294

Praveen Kumar B, Vialard J, Lengaigne M, Murty VSN, McPhaden MJ (2012) TropFlux: air–sea fluxes for the global tropical oceans—description and evaluation. Clim Dyn 38:1521–1543. doi:10.1007/s00382-011-1115-0

Saji NH, Yamagata T (2003) Possible impacts of Indian Ocean dipole mode events on global climate. Clim Res 25:151–169. doi:10.3354/cr025151

Saji NH, Goswami BN, Vinayachandran PN, Yamagata T (1999) A dipole mode in the tropical Indian Ocean. Nature 401:360–363. doi:10.1038/43854

Spencer H, Sutton RT, Slingo JM, Roberts JM, Black E (2005) The Indian Ocean climate and dipole variability in the Hadley centre coupled GCMs. J Clim 18:2286–2307

Susanto RD, Gordon AL, Zheng Q (2001) Upwelling along the coast of Java and Sumatra and its relation to ENSO. Geophys Res Lett 28(8):1599–1602

Thompson B, Gnanaseelan C, Salvekar PS (2006) Variability in the Indian Ocean circulation and salinity and its impact on SST

anomalies during dipole events. J Mar Res 64:853–880. doi:10.1357/002224006779698350

Thompson B, Gnanaseelan C, Parekh A, Salvekar PS (2009) A model study on oceanic processes during the Indian Ocean Dipole termination. Meteorol Atmos Phys 105:17–27. doi:10.1007/s00703-009-0033-8

Tokinaga H, Tanimoto Y (2004) Seasonal transition of SST anomalies in the tropical Indian Ocean during El Niño and Indian Ocean dipole years. J Meteorol Soc Jpn 82:1007–1018. doi:10.2151/jmsj.2004.1007

Uppala SM et al (2005) The ERA-40 re-analysis. Q J R Meteorol Soc 131:2961–3012. doi:10.1256/qj.04.176

Vinayachandran PN, Saji NH, Yamagata T (1999) Response of the equatorial Indian Ocean to an unusual wind event during 1994. Geophys Res Lett 26:1613–1616. doi:10.1029/1999GL900179

Webster PJ, Moore AW, Loschnigg JP, Leben RR (1999) Coupled ocean atmosphere dynamics in the Indian Ocean during 1997–1998. Nature 401:356–360. doi:10.1038/43848

Yamagata T, Behera SK, Luo JJ, Masson S, Jury MR, Rao SA (2004) Coupled ocean–atmosphere variability in the tropical Indian Ocean. In: Wang C, Xie SP, Carton JA (eds) Earth climate: the ocean–atmosphere interaction. Geophys Monogr Ser 147:189–211. AGU, Washington. doi:10.1029/147GM12

Yatagai A, Kamiguchi K, Arakawa O, Hamada A, Yasutomi N, Kitoh A (2012) APHRODITE: constructing a long-term daily gridded precipitation dataset for Asia based on a dense network of rain gauges. Bull Am Meteorol Soc 93:1401–1415